DONALD D. DUNCAN

OPTICS IN BIOMEDICAL ENGINEERING

Two biomedical engineering projects that have benefited from recent advances in optical technology are discussed. In one project, laser Doppler measurement techniques are used to quantify the dynamics of realistic fluid flows within casts of human arteries. In the other, a fiber-optic interferometer is being developed to measure very small movements of the components of the middle ear.

INTRODUCTION

Biomedical programs at APL involve a broad range of applications of varied optical technologies. Typically, such applications have been with departments of the Johns Hopkins Medical Institutions (JHMI) and include (1) laboratory experimentation with and modeling of the scatter and absorption of infrared radiation within the head as a means of inferring blood oxygenation and metabolic rate, and making measurements of light absorption by human hemoglobin in the visible wavelength regime (Department of Anesthesiology); (2) developing equipment to quantify the electrokinetic behavior of mammalian cochlear outer hair cells (Department of Otolaryngology); and (3) developing (current project) an angiography technique using fluorescent organic dyes (Department of Medicine). Although concepts that were familiar to the optical engineer of 50 years ago were used in each of these projects, all of the concepts have been improved upon by developments in optical technologies that have taken place within the last five years.

Space does not permit all of the projects mentioned to be discussed to the depth that each deserves; therefore, two projects that best exemplify APL's recent involvement in biomedical engineering have been chosen for detailed examination.

USE OF LASER DOPPLER VELOCIMETRY TO MEASURE FLOW IN MODELS OF HUMAN BLOOD VESSELS

Background

Indirect evidence indicates that fluid dynamics plays a role in atherogenesis (beginnings of arterial disease). Although this role is presumed to reflect a response of the vessel wall to the adjacent flow field, the local fluid-dynamic behavior is obviously influenced by the geometrical configuration of the vessel. It is thought, therefore, that geometrical factors play an important role in atherosclerosis (deposition of fatty materials within the vessel).[1] Efforts aimed strictly at correlating geometrical factors and arterial occlusion do not account for the actual mechanisms involved. Characterizing the fluid-dynamic environment near the vessel wall can provide important clues to the physical processes involved in atherosclerosis, and laser Doppler velocimetry (LDV) is a powerful tool for making this characterization.

The experimental procedure we use is to create a model of a segment of artery, subject the model to a physiologically realistic pulsed flow wave (to simulate the heart beat), and measure the flow variables near the wall of the model. This procedure results in a model that is an improvement over most earlier physical models, which were simply rigid cylindrical tubes or flow-through casts. Although it has been argued that neglecting vessel-wall compliance in the earlier models is unimportant to the fluid dynamics at the wall, such arguments are based primarily on theoretical analyses and experimental measurements of fluid flow within cylindrical tubes. Despite such arguments, few experimental results support extending them to (for example) arterial branchings, even though many fatty deposits are observed to occur in these branching geometries. Furthermore, recent work[2] suggests that the compliance of the vessel wall can have a marked effect on shear rates. Our experiments examined the near-wall fluid dynamics in realistically compliant models of human arteries.

Methods Used in Making the Model

Our previous measurements were generally made using rigid casts of human aortic bifurcations. The preparation of these rigid casts and the measurement techniques used to obtain data from them are described elsewhere.[3,4] The preparation of the compliant model of the aortic bifurcation used in this study is described here.

While the arterial segment was fixed at physiological pressure, it was injected with a silicone rubber compound that vulcanizes at room temperature. The compound was allowed to cure until vulcanization was complete and then the silicone rubber casting, which was a replica of the vessel interior, was removed.

A two-piece plaster of paris mold was formed around the rubber casting. This plaster mold replicated the internal contour of the original vessel. A metal having a low melting point was poured into the plaster mold to produce a metal copy of the rubber casting.

The metal casting was coated with a paint-like compound until the thickness of the coating corresponded to the wall thickness desired for the compliant cast. Next a two-piece plaster of paris mold was formed around the coated casting in the same way as had been done with the silicone rubber casting. This second plaster mold es-

tablished the contour of the outside of the final cast. The metal casting was stripped of the paint-like layer and was positioned inside the second plaster mold. The final step was to pour a two-part, transparent, elastic silicone rubber compound into the plaster mold that surrounded the metal casting. The elastic modulus of the rubber used in this final casting is in the range of published values for human arteries.[5] After the rubber casting was cured, the mold was separated from it and the metal casting was melted out by hot water.

The compliant cast replicated the original arterial segment. This cast was mounted in a Plexiglas box to which was added a sodium thiocyanate solution whose refractive index was matched to the refractive index of the cast (see Fig. 1). The same fluid was used in the flow system described next.

A pulsed fluid flow (of zero average flow) was generated by a cam-driven piston pump operated in parallel with a metering pump that provided the steady flow. The cam design was based on measurements of flow in human abdominal arteries. The modeled arterial segment (the cast) was preceded by a straight section of tubing with an inside diameter that was matched to the diameter of the cast entrance and of a sufficient length to ensure that flow at the cast entrance was fully developed. (By fully developed flow we mean that the fluid velocity attained a parabolic profile across the tube cross section, characteristic of a nonturbulent flow within a cylindrical tube.) Setting up these conditions ensured that the fluid dynamic environment within the model would not be affected by small geometrical details of the flow system.

Once the above conditions were established, an LDV technique was used to measure instantaneous velocities near the walls of the cast. The specific equipment used was a commercial LDV system that included a helium-neon laser (0.6328-μm wavelength) operated in the backscatter mode with a nominal 10.75° beam-crossing angle (in air). The velocity of the fluid was estimated in a sample volume that approximated that of an ellipsoid
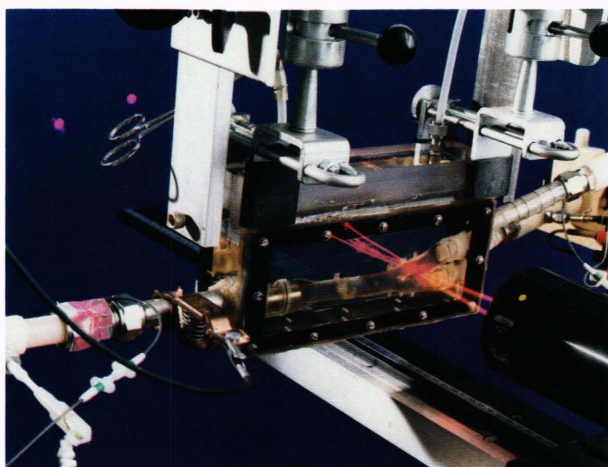
Figure 1—Plexiglas box containing compliant cast of a human aortic bifurcation. Fluid flow is from right to left, the left iliac artery is at the top of the picture, the right is at the bottom.

of revolution measuring 300 × 55 μm. Within the sample volume, the two intersecting beams created a series of "fringes" that were separated according to the formula

$$s = \lambda/[2 \sin (\theta/2)] , \qquad (1)$$

where θ is the beam-crossing angle and λ is the wavelength. The fringe spacing was 3.38 μm for the 10.75° beam-crossing angle used. Because the local refractive index was higher than that of air, the beam-crossing angle within the cast was actually somewhat less than the angle measured in air. The difference in refractive index could cause one to assume that the fringe spacing was actually greater than 3.38 μm, but it must be remembered that the wavelength of the light is also decreased within the medium having the higher refractive index (the fluid); therefore, the net effect is that the local refractive index has no effect on the magnitude of the Doppler shifts created by the moving particles.

The flow was seeded with 5.2-μm diameter polystyrene microspheres to make the backscatter signal stronger. As the particles flowed through the fringe pattern within the sample volume, the observed scatter was temporally modulated at a frequency shift of,

$$f_D = v/s , \qquad (2)$$

where v is the component of the particle velocity perpendicular to the fringes and s is the fringe spacing determined in Eq. 1. The assumption made here was that the particle follows the fluid flow so that the particle velocity accurately reflects the fluid velocity. Note that if the light scattered from the moving particle is viewed as undergoing a Doppler shift that is proportional to the sine of the angle between the normal to the velocity vector and each incident laser beam, the conditions would be satisfied by exactly the same equation as the one above for the observed frequency f_D; therefore, the fringe paradigm and the Doppler model of the phenomenon are entirely equivalent.

Resolving the ambiguities in flow direction was one of the achievements of the optics design. This was accomplished by shifting the frequency of one of the laser beams 40 MHz by means of an acousto-optic Bragg cell. The process can be thought of as causing the fringes to move so that a bias is imposed on the frequency of the observed scatter signal. Then, if the particles are stationary, only the bias frequency is observed, but particle movement counter to the direction of the fringe movement adds to the bias frequency and particle movement in the direction of the fringe movement subtracts from it. In this way, negative as well as positive flow velocities were measured. Since the expected Doppler shifts were a small fraction of the bias frequency, the detected signal was channeled through a down-converter to give

an effective bias frequency of 50 kHz before it was passed to the processing electronics.

The reason for matching the refractive index of the working fluid to that of the compliant cast is twofold. First, we wanted the position of the beam crossing to be determined only by the position of the external LDV system, regardless of the angle at which the laser beams entered the compliant cast. Such would not have been the case had the refractive index of the working fluid not been matched to that of the cast. Furthermore, had the indexes not been matched, the sample volume would have wandered about as the wall of the vessel moved in response to the pressure wave. (In an extreme case of geometrical configuration and mismatched index, it is possible for the beams not to cross and, therefore, there would be no sample volume.)

Data acquisition equipment included a counter-type signal processor, an analog-to-digital converter, and a personal computer. By triggering the analog-to-digital unit with a signal derived from the cam that generated the pulsed flow, a number of cycles of the velocity waveforms were acquired and recorded. The waveforms were subject both to a number of noise sources and to uncertainties caused by the low data rates at low velocities. The mass flow rate of fluid through the measurement volume is strictly a function of the fluid velocity. It can be assumed that the data rate will be proportional to the fluid velocity, if the concentration of seeding particles can be assumed to be constant. Therefore the variance of the velocity estimate is inversely proportional to the velocity.

Averaging the data from successive pulses effectively reduces the noise and uncertainty associated with the low data rates, but in counter-based systems such as the one that was used here, the Doppler shift (and therefore the velocity) of a single particle traversing the LDV sample volume is determined from the length of time required for a specified number of zero crossings of the signal "burst" (see Fig. 2).[6] If the length of time is less than a preset value (as could result from noise), the output of the counter is set to zero, resulting in a dropout in the velocity waveform. If only the average waveform is recorded, the presence of the dropouts will be obscured by the averaging operation, but the velocities will be underestimated. In the present case, dropouts seemed to be caused by temporal modulation of the scatter from the wall of the compliant cast. This problem was exacerbated by deposits that accumulated over a period of time on the inside surface of the cast.

Latching is another problem associated with data gathering. The system is designed for low data rates and its output remains fixed at the previous value until the next burst is detected. (This behavior is typical of counter-type systems.) As a result, the leading edge of a velocity waveform will almost always be biased somewhat downward, while the trailing edge will be biased upward. By recording the individual velocity pulses, it was possible to detect and correct both for dropouts and for latching. Furthermore, because an ensemble of velocity traces was acquired, the velocity variance at each

point of the waveform could be calculated. This technique thus provided estimates of the pulsed velocity waveforms and estimates of the inaccuracy.

A line-scan camera interfaced to the computer was used to measure wall motion. Light from a linearly polarized helium-neon laser was formed into a slit and passed transversely through the arterial cast at the sites of interest by means of a cylinderical lens and beam-expander optics. The silhouette of the cast cross section was projected onto the 512-element detector array. To put the images of the internal and external sides of the cast wall within the dynamic range of the camera, the light intensity was adjusted by changing the orientation of a polarizer placed immediately in front of the camera. A signal from the cam that generated the pulsed flow was also used here to trigger data acquisition. The camera elements were read out every 8 ms and the motion of the inner surface of the cast at each site was obtained by taking the average over a number of pump cycles. After data for the pulsed flow had been taken, the piston pump was turned off and the wall position recorded. The two data sets provided an estimate of the instantaneous wall position that later was used in conjunction with the velocity data to calculate shear rates.

To estimate shear rates near the vessel wall at a specific site, temporal velocity waveforms were measured at three nominal (zero flow) distances from the site: 0.51, 0.76, and 1.02 mm. Once pulsed flow began, these distances changed with time and were computed using the data from the wall-motion measurement system. At each 8-ms interval, the three velocity estimates were fit by least-squares to a second-degree polynomial, the instantaneous distance from the wall being the independent variable (assuming zero velocity at the wall). For this model, the coefficient of the linear term is an estimate of the instantaneous shear rate at the wall. The temporal shear waveform at each site was estimated in this way. Subsequent data processing provided various measures of shear rate, including peak positive and negative shears,
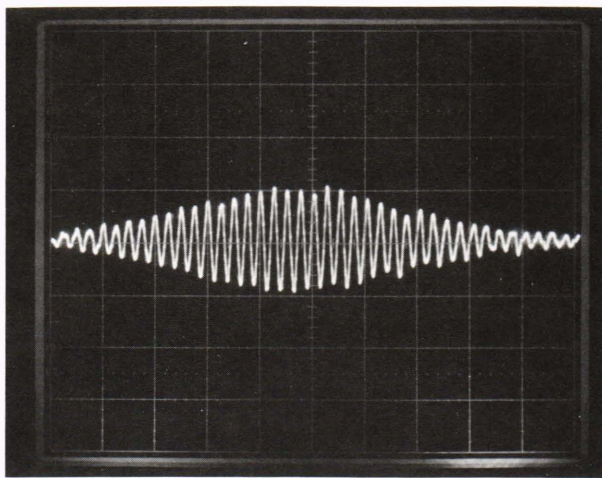
Figure 2—Typical Doppler "burst" caused by a single particle flowing through the sample volume. High-pass filtering causes the signal to be symmetrical about the abscissa.

fraction of pulse displaying positive shear, etc., which have been described elsewhere.[7] Only mean (i.e., average over the pulse period) shear-rate results are presented here.

Results

Synthetic clove oil (eugenol) was used as the working fluid in the experiments with rigid casts.[3] Because the viscosities of the working fluids for experiments in rigid and compliant casts differed, the flow rates and pulse frequencies for each experiment were adjusted to provide identical Reynolds and unsteadiness numbers. The Reynolds number, Re, which provides a means of characterizing a flow (of a gas or fluid), is a nondimensional number given by the formula

$$Re = v \, d/\nu \; , \qquad (3)$$

where v is the mean velocity, d is the transverse dimension of the vessel, and ν is the kinematic viscosity. Reynolds members are important in this work because their use allows flows to be characterized as either laminar or turbulent. Typically, flow can be considered laminar for Reynolds numbers smaller than about 2000. Unsteadiness, α, another nondimensional number, is given by

$$\alpha = (d/2)(2\pi/\nu T)^{1/2} \; , \qquad (4)$$

where T is the pulse period. This parameter is useful because the ratio $d/2\alpha$ is the thickness of the oscillating boundary layer. In the present work, these two parameters were, respectively, 750 and 11, where d was the diameter of the aorta (approximately 15.2 mm).

A typical velocity history with estimated uncertainties is shown in Fig. 3. This particular waveform, measured at a distance of 0.51 mm normal to the wall at site 1 (see Fig. 4), was produced by averaging the velocity waveforms resulting from 32 pressure pulses. The larger error bands on the trailing edge of the waveform reflect the latching phenomenon mentioned previously. Marked flow reversals, as observed at this site, were typical of all sites surveyed.

The measured wall motion at site 1 is illustrated in Fig. 5. For this case, the maximum radial movement was approximately 1.5% of the diameter of the vessel interior (lumen). At other sites the movements were as high as 10.8%. These wall movements comprise translation and strain components. For the cast as a whole, strains ranged between 2% and 4%.

The history of the shear rate ($\partial v/\partial r$) at site 1 is presented in Fig. 6. The data were obtained from the velocity profile shown in Fig. 3, the additional velocity profiles at nominal distances of 0.76 and 1.02 mm, and the wall motion data from Fig. 5.

Figure 7 is a plot of the mean shear rate (averaged over the shear history) at each site in the rigid cast versus the value at the corresponding site in the compliant cast. For each of these experiments, the fluid shear rates have been
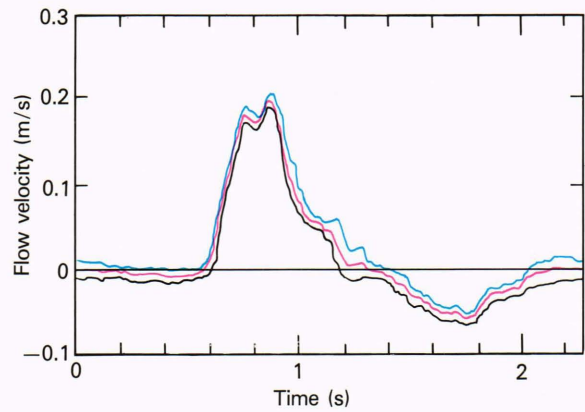
Figure 3—Velocity waveform with $\pm 1\sigma$ confidence intervals. Data taken 0.51 mm from the wall at site 1.
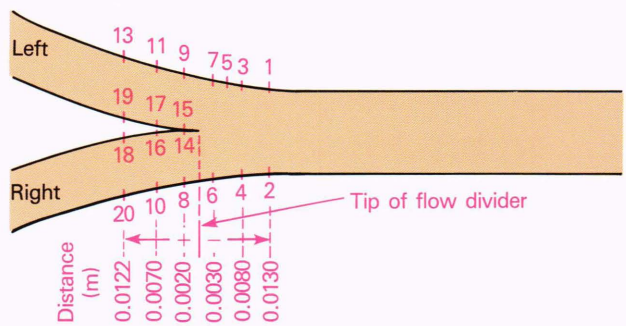
Figure 4—Silhouette of aortic bifurcation, indicating sites and their axial distances from the tip of the flow divider.
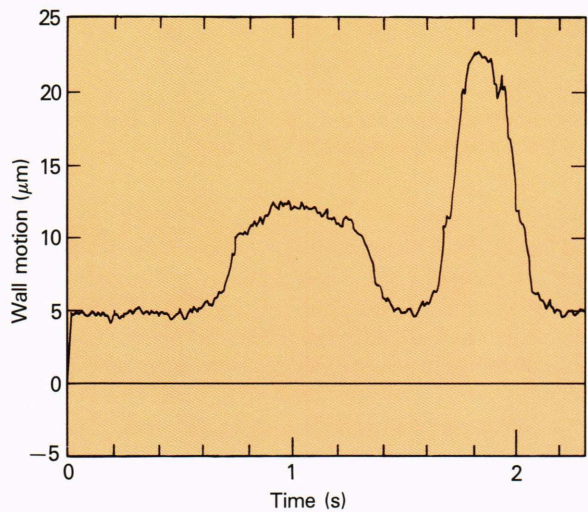
Figure 5—Wall motion at site 1. The zero ordinate value corresponds to the wall position at steady flow.

normalized to a kinematic viscosity of 4×10^{-6} m^2/s, which is approximately that of blood at high shear rates. Note that these points fall roughly into two groups. The two groupings correspond to the sites along the lateral walls and those at the flow-divider walls. Within the former group the correlation coefficient is 0.62 ($p \leq 0.02$) and for the latter, 0.90 ($p = 0.02$).
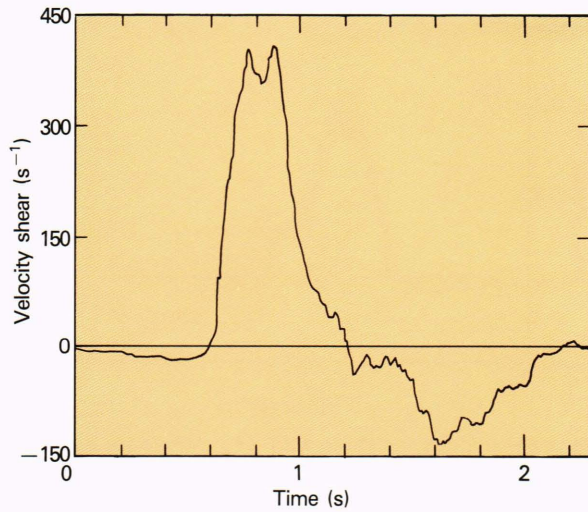
Figure 6—Shear rate ($\partial v/\partial r$) history at site 1.

Figure 8—Illustration of the human ear (from Plate 15, p. 524 of Ref. 9). ©1988, W. B. Saunders Co; reprinted with permission.
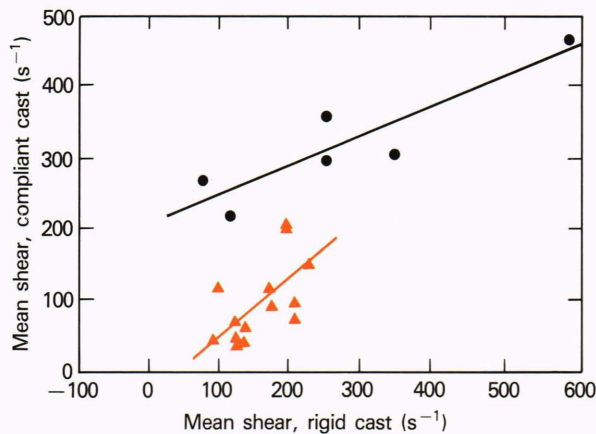

Figure 7—Mean shear rates in rigid and compliant casts. Sites along the flow divider are indicated by dots (•), those along the lateral walls by triangles (▲).

The results suggest that the effect of vessel compliance is to decrease wall shear rates along the lateral walls and to increase shear rates at the flow-divider walls, where the rates are already markedly higher. The phase relationship between the velocity waveform and the wall motion seems to be the factor that determines whether vessel compliance increases or decreases fluid shear. We are now pursuing a frequency analysis of these data to confirm this hypothesis.

Because others (e.g., Ref. 8) have shown that the non-Newtonian nature (i.e., viscosity as a function of velocity shear) of blood can have a marked effect on the near-wall shears, our present efforts include experiments using a non-Newtonian working fluid prepared by adding a small amount of a synthetic polymer (Separan AP-30) to the aqueous sodium thiocyanate solution.

The reader is referred to Friedman[1] for more detail on the implications of the experimental results described here and on the links between atherosclerosis and the dynamics of blood flow.
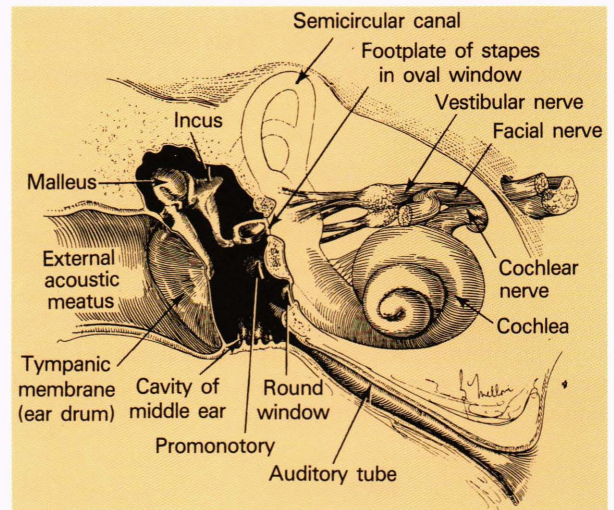
A FIBER-OPTIC INTERFEROMETER FOR MEASURING MOVEMENTS WITHIN THE MIDDLE EAR

Background

A diagram of the human hearing apparatus[9] is shown in Fig. 8. The middle ear—that is, the region between the ear drum (tympanic membrane) and the sensory organ (cochlea)—is a mechanical device that matches the impedance of the environmental air to the fluids within the cochlea. The hammer, anvil, and stirrup (malleus, incus, and stapes) are the three major components of the middle ear and constitute the ossicular chain. One end of the malleus is attached to the tympanic membrane (a thin disk-shaped membrane about 1 cm in diameter) and the other end is attached by ligaments to the incus, which, in turn, is attached to the stapes. The footplate of the stapes, which is roughly 1.5 × 3 mm, is attached to the oval window of the cochlea.

In a wide variety of diseases, this ossicular chain becomes damaged, producing a significant hearing loss. Microsurgical repair of the mechanical linkage with autogenous or prosthetic materials is successful in many cases, especially when the defect is not severe. For example, in 80% of cases, conductive hearing losses in ears with a damaged incus but with an intact stapes arch can be corrected to within 10 dB of normal hearing thresholds.[10]

Nevertheless, no means are presently available to evaluate objectively a middle-ear reconstruction procedure other than audiometric testing after healing has occurred. Immediate intraoperative assessment of the mobility of individual parts and/or the completely reconstructed ossicular chain would be an invaluable adjunct to this kind of surgery. Therefore the objective of this research is to develop technology for use intraoperatively to measure ossicular mobility (e.g., stapes footplate, malleus, or ossicular prosthesis) resulting from acoustic

stimuli, and for use as a research tool for studying middle-ear mechanics. As a research tool, the device would be used to evaluate the design and placement of middle-ear prostheses and the effect of intervening tissue layers between a prosthesis and the remaining parts of the ossicular chain. This project is interesting from both an engineering and a biological standpoint. It unites concepts in electromagnetic interference that have been known and used for nearly 300 years with the more modern technological advances such as fiber optics, optical elements with gradient refractive index, heterodyne detection, etc.

Methods that have been used in the past to detect small vibrations in various parts of the auditory system include capacitive probes,[11] Mössbauer-effect velocity sensors,[12] laser interferometry,[13] time-averaged holography,[14] SQUID magnetometry,[15] and video-enhanced microscopy.[16] These approaches contributed valuable physiologic data, but have not yet been applied to clinical situations. For each of these methods either spatial resolution is limited or extended time is required for data collection or data processing.

Our approach has been to develop a laser interferometer based on the Mach–Zehnder configuration. This particular configuration allows the greatest flexibility for implementation, provides good signal-to-noise characteristics, and does not impose unreasonable demands on specific details of the application such as would be the case for the Fizeau[17] or Sagnac[18] interferometers. Preliminary experiments convince us that 0.1-nm resolution is attainable; that the effects of background noise can be minimized using coherent detection techniques; and that the measurements can be made quickly enough to minimize the effects of relative subject/probe movement. Furthermore, there are other possible applications (e.g., nondestructive evaluation of materials) for a device that has these capabilities.

Ordinarily, interferometric devices cannot be applied to clinical and operating-room conditions because of major technical problems. These problems include background noise, relative movement between the subject and the instrument probe, low tissue reflectivity, and uncertainty as to whether the operative exposure of the middle-ear structures will invalidate the data. An additional problem is that the measurements to be made are within a restricted volume and the movements are very small (e.g., the extent of movement of the footplate of the stapes at the threshold of hearing is only a few tenths of a nanometer). These problems are addressed by our laboratory demonstration system.

Development of a Method

Our original design was based on a heterodyne Michelson interferometer, using a helium-neon laser, a number of bulk optical components, and a fiber-optic probe. We constructed such a device and found it to have several shortcomings. We replaced this system by a Mach–Zehnder interferometer, which is more refined and has an actively stabilized reference leg and a more sophisticated signal-processing scheme that provides absolute target excursion estimates continuously without needing periodic calibration. We describe here the current system and the preliminary measurement results obtained with it.

The concept of interferometry is best understood through a discussion of the classical Michelson interferometer (see Fig. 9). A beam-splitter is used in this type of interferometer to separate a beam of light into two components—one reflected from a target and the other reflected from a reference mirror. The same beam-splitter then recombines the two beams so that they both fall onto the detector. When the target moves, the detector signal moves through a light-dark-light (constructive-destructive-constructive interference) transition as the relative lengths of the two arms of the interferometer change by one-half wavelength. The target motion can then be deduced by counting these light-dark fringes.

The varying portion of the light intensity at the output of an interferometer can be expressed by

$$I_d \propto \cos (2ka) , \tag{5}$$

where I_d = irradiance at detector, k = source wavenumber $(2\pi/\lambda)$, and a = physical path difference between the source and reference arms of the interferometer.

From Eq. 5 it can be seen that the output signal completes a single light-dark transition for a path difference of one-half wavelength or a target excursion of one quarter wavelength (158.2 nm, at the helium-neon wavelength of 632.8 nm). Since the objective is to measure much smaller target excursions than 158.2 nm, we see that the resulting detector output will be very small deviations about some operating point on the curve described by Eq. 5. For the signal-to-noise characteristics to be optimum, however, the interferometer must operate at the so-called quadrature point,[19] that is, the point at which the physical path difference is some odd multiple of quarter wavelengths; this is the optimum operating point.

The general form of the Mach–Zehnder interferometer is illustrated in Fig. 10. Operation of this interferome-
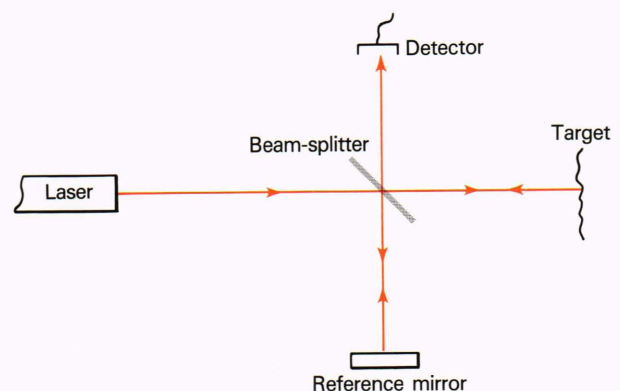
Figure 9—Illustration of the classical Michelson interferometer. The single beam-splitter both splits and recombines the signal and reference beams.
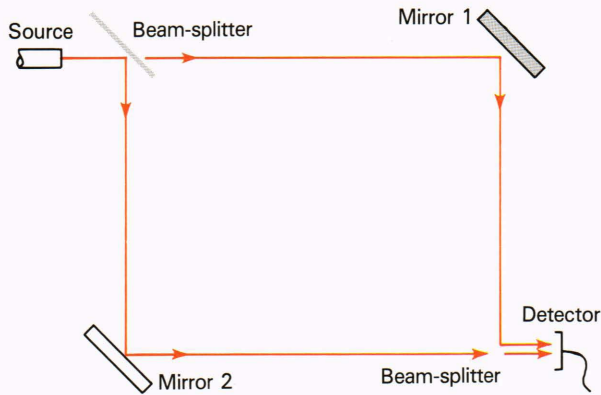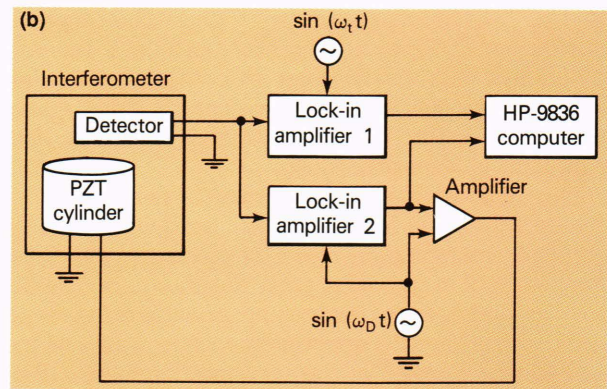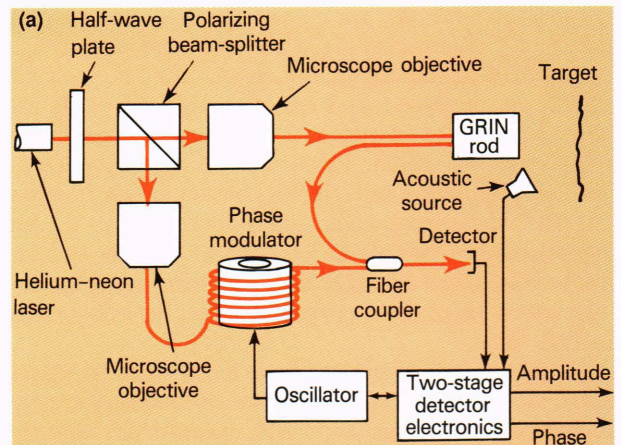
Figure 10—Illustration of Mach–Zehnder interferometer. Separate beam-splitters split and recombine the signal and reference beams.

Figure 11—(a) Simplified schematic of the fiber-optic interferometer. The half-wave retardation plate and the polarizing beam-splitter allow the energy balance between the signal and reference beams to be controlled. Microscope objectives couple light into monomode fibers. Several turns of fiber around a PZT tube (phase modulator) permit the interferometer's optical path difference to be modulated. The GRIN-rod probe efficiently couples light from the sending optical fiber, off the target surface, and into the receiving optical fiber. The fiber-optic coupler mixes the signal and reference beams. (b) The system for achieving active feedback stabilization of the interferometer operating point. A DC level is superimposed on the reference dither signal to compensate for drift from the quadrature operating point. The dither and target excitation frequencies are ω_D and ω_t, respectively.

ter is conceptually the same as that of the Michelson except that separate beamsplitters are used to split and recombine the signal and reference beams. Our implementation of the Mach–Zehnder interferometer is shown schematically in Fig. 11. The system contains a few bulk optical components and is composed mainly of monomode optical fiber. (Monomode means that the fiber will propagate only a single spatial mode.) The result is that the optical path length of the fiber is unique, an important quality because the finite coherence length of the source requires the signal and reference arms of the interferometer to be of nearly equal optical path length. Furthermore, for the signal and reference fields to interfere, they must be polarized alike. (Observe that this fiber must not only be monomode, but must be of a type that preserves polarization).[20] In ordinary monomode optical fibers, fluctuations in the polarization of the light can be produced by temperature fluctuations or bends in the fiber.[21] A polarization-preserving fiber is designed so that the polarization components of the fields propagating within the fiber do not mix. The result is that this type of fiber can be bent though short-radius curves or subjected to temperature fluctuations (such as those that result from handling) without inducing polarization noise.

Several turns of the optical fiber were wrapped around a piezoelectric cylinder (a lead–zirconate–titanate ceramic commonly called a "PZT" cylinder) to provide a means of controlling the interferometer operating point precisely. By applying a low voltage to the PZT cylinder, the tube is caused to expand and stretch the fiber and so change its optical length.

Figure 11a also shows the design for the interferometer probe tip. The configuration uses a graded refractive index (GRIN) rod and two polarization-preserving fibers. A GRIN rod is an optical element in which the refractive index varies radially from the optical axis parabolically, causing the light rays to follow a sinusoidal trajectory within the rod. Therefore, a lens of any desired focal length can be effected simply by cutting the rod to the appropriate length. In this probe-tip design, the laser energy was delivered through one fiber and received

through another. The advantage of such an arrangement was that the polarizations of the beams could be maintained by initially aligning the two optical fibers correctly. This particular design used a GRIN rod that produced a collimated beam. Analyses based on physical optics predicted that this configuration would be least sensitive to the nominal probe/target separation. Furthermore, for highly specular targets, the design provided good coupling efficiency, that is, a large fraction of the light emitted by the probe was reflected by the target and coupled back into the receiving fiber.

In the classical Mach–Zehnder configuration, one beam-splitter is used as a splitter and another is used as a combiner. In our design, the combining was accomplished by means of a fiber-optic coupler. Ideally, a polarization-preserving fiber-optic coupler would be used

for this purpose. We were constrained by cost considerations to use a low birefringence monomode coupler. To increase the coupling efficiency to its maximum, we formed fiber-optic quarter- and half-wave retarders (i.e., waveplates) by looping the coupler leads through bends having the appropriate radius.[22]

The optical components of the actual demonstration unit of the fiber-optic interferometer are visible in Fig. 12. The waveplates are the loops of copper tubing at the middle right. The PZT cylinder is to the left of the waveplates. The probe tip is in the foreground, hidden behind the PZT-driven mirror used in calibrating the interferometer.

System tests showed that the heterodyne detection scheme was extremely sensitive to low-frequency drift in the optical path difference of the interferometer, but the system operating point could be actively stabilized by the PZT tube within the reference leg. A low-frequency (200 Hz) "dither" signal was imposed on the PZT, and the resultant signal component at this frequency was detected coherently to provide a feedback signal. The feedback loop (shown in Fig. 11b) provides compensation both for low-frequency system noise and for slow movement of the probe tip.

Another feature of the signal processing scheme is a continuous calibration technique.[13] When the detected signal is expanded in terms of its harmonic content, the expansion reveals that the signal amplitudes at the fundamentals of the target-excitation and dither frequencies are, respectively,

$$C_t(a) = C \sin(\phi) J_1(2ak) J_0(\pi) \qquad (6a)$$

and

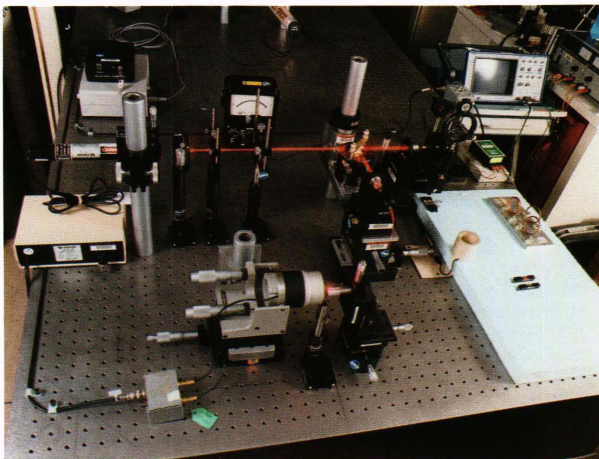$$C_D(a) = C \sin(\phi) J_0(2ak) J_1(\pi) , \qquad (6b)$$

where C is a system-dependent constant, ϕ is the optical phase difference between signal and reference legs of the interferometer, a is the amplitude of (periodic) target displacement, and J_n is the Bessel function of the first kind and of order n. A ratio of the two signal components depends only on the displacement amplitude of the target and the known amplitude modulation of the reference leg. All dependence on the relative signal/reference phase and the absolute signal amplitudes cancels, thereby absolute displacement estimates are provided that are insensitive both to variations in the relative intensities of the interfering beams and to small fluctuations in the stabilized optical path distance.

Results

Preliminary tests of this system used a PZT-driven mirror as a target. For a heterodyne interferometer, as pointed out in the expression for the signal amplitude, the calculated target movement versus the actual excursion bears the form of the first-order Bessel function of the first kind. Our measurements reproduced this operating characteristic to within ±3.5 dB down to the system noise level of approximately 0.41 nm. This measurement is plotted in Fig. 13. An ordinate value of −50 dB represents an actual displacement of 0.294 nm; 0 dB represents a displacement, a_E, of 92.897 nm (the maximum target motion for which the interferometer produces an unambiguous motion estimate).

Convinced that the system could provide reasonable estimates of target excursion, we attempted to perform measurements on the fresh tympanic membrane from a human cadaver. Unfortunately, the reflectivity of the tympanic membrane was too low to be compatible with the current design of the collimated probe beam, so the signal obtained was not of sufficient amplitude to be measured directly. To overcome this problem, a 1.4-mg sliver of mirror was mounted on the tympanic membrane at the umbo. Displacement amplitudes were measured over a broad range of the acoustic frequencies. To get
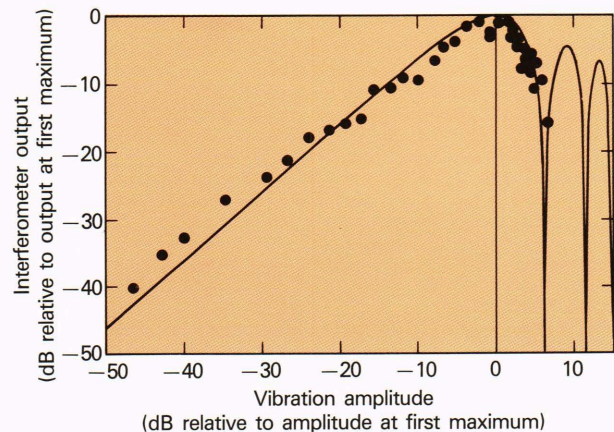

Figure 12—Layout of the optical components of the fiber optic interferometer.

Figure 13—Interferometer output as a function of target excursion. The solid curve is the theoretical characteristic; the points represent actual measurements. The ordinate is 20 log [$J_1(2ka)/J_1(2ka_E)$]; the abscissa is 20 log (a/a_E), where a_E is the displacement at the first maximum of J_1.

an indication of the system stability, 10 measurements (plotted in Fig. 14) were made for each discrete frequency interval. These measurements compare well with measurements made by Vlaming and Feenstra.[23] Measurements of this kind were also made using a 0.6-mg mirror sliver mounted on the arch of the stapes. Results from one pilot experiment are shown in Fig. 15. To verify that the stapes was in motion, and not the entire specimen, a measurement was also made on a fixed portion of the mastoid.

Further experiments under more nearly normal physiologic conditions are necessary before we can attempt to interpret the frequency dependence of the ossicular motion. The dynamic range and frequency bandwidth of the stabilization scheme must still be addressed. These requirements are imposed by hand tremor. There is, in the literature, a reasonable amount of data on the frequency content of hand tremor,[24] but little quantitative data on the magnitude of the movement. In light of this paucity of information, finding means of measuring typical hand tremor under various conditions of arm, wrist, and hand support has been set as an objective. At present we use a hand-held probe to which is attached an optical fiber illuminated by a light-emitting diode to make these measurements. The probe is held within the field of an operating microscope that has an attached video tape recorder. Various image-processing techniques such as sequential frame differencing and thresholding will provide movement estimates at the 30 Hz video frame rate.

Measurements made with the devices we have developed so far have demonstrated several concepts that are essential to the eventual development of a device that can make all desired measurements. Such a device would be fiber-optic based and would produce a real-time estimate of the target excursion and phase in response to an acoustic stimulus. Future refinements of the current design could include integrated-optics phase shifters and radio-frequency heterodyning.

Figure 14—Displacement amplitude of fresh human tympanic membrane: A 1.4-mg mirror sliver is located at the umbo; spectral displacement amplitude, 79 dB sound pressure level; probe/target separation, 3 mm.

Figure 15—Displacement amplitudes of (a) mastoid and (b) stapes/mastoid difference. A 0.6-mg mirror sliver is mounted on the crural arch; spectral displacement amplitude, 79 dB sound pressure level; probe/target separation, 3 mm.

REFERENCES

[1] M. H. Friedman, "Geometric Risk Factors for Arteriosclerosis," *Johns Hopkins APL Tech. Dig.* **4**, 85-95 (1983).

[2] J. M. Tarbell, M. Klanchar, and A. Dutta, "Effects of Phase Relationships on Wall Shear Stress in Curved and Straight Elastic Artery Models," in *The Role of Blood Flow in Atherogenesis*, Y. Yoshida et al., eds., Springer-Verlag, Tokyo, Japan, 103-108 (1988).

[3] M. H. Friedman, G. M. Hutchins, C. B. Bargeron, O. J. Deters, and F. F. Mark, "Correlation of Human Arterial Morphology with Hemodynamic Measurements in Arterial Casts," *J. Biomech. Eng.* **103**, 204-207 (1981).

[4] M. H. Friedman, C. B. Bargeron, G. M. Hutchins, F. F. Mark, and O. J. Deters, "Hemodynamic Measurements in Human Arterial Casts, and Their Correlation with Histology and Luminal Area," *J. Biomech. Eng.* **102**, 247-251 (1980).

[5] G. J. Langewouters, K. H. Wesseling, and W. J. A. Goedhard, "The Static Elastic Properties of 45 Human Thoracic and 20 Abdominal Aortas in Vitro and the Parameters of a New Model," *J. Biomech.* **17**, 425-435 (1984).

[6] F. Durst, A. Melling, and J. H. Whitlaw, *Principles and Practice of Laser-Doppler Anemometry*, 2nd ed., Academic Press, New York, pp. 241-280 (1981).

[7] O. J. Deters and M. H. Friedman, "Correlation Among Shear Rate Measures in Vascular Flows," *J. Biomech. Eng.* **109**, 25-26 (1987).

[8] D. Liepsch, "Laser-Doppler-Measurements in True-to-Scale Human Elastic Models with Newtonian and Non-Newtonian Fluids," ASME *Forum on Unsteady Flows in Biological Systems*, pp. 29-32 (1985).
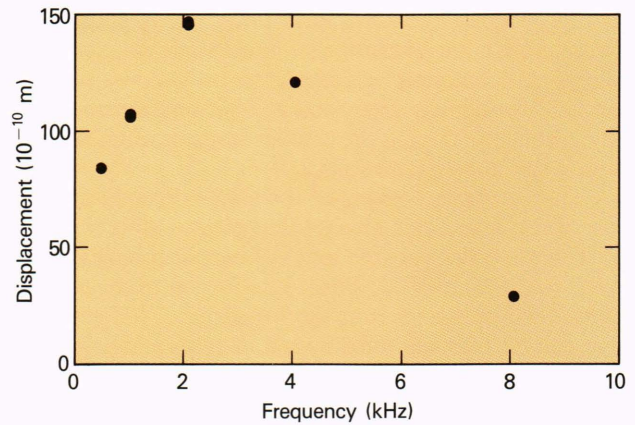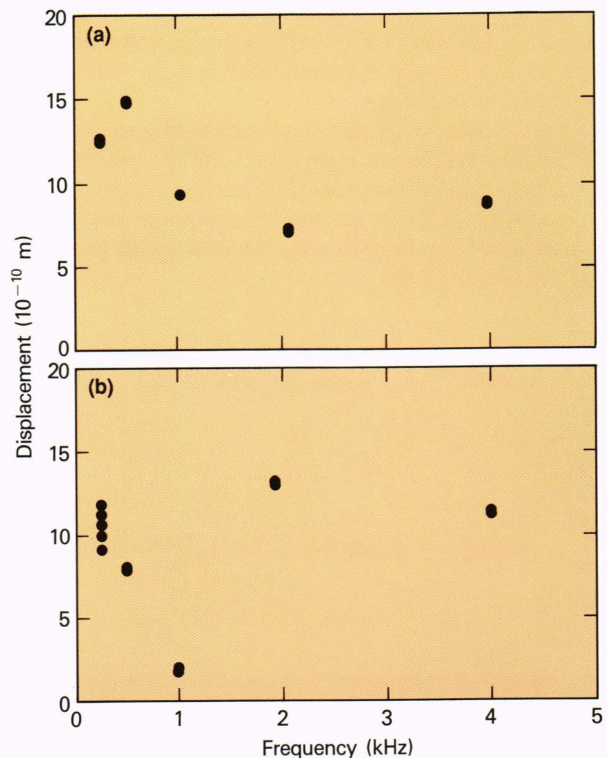
[9] *Dorlands Illustrated Medical Dictionary*, 27th ed., W. B. Saunders Co., Philadelphia, Plate 15, p. 524 (1988).

[10] J. L. Sheehy, "Personal Experience with TORPS and PORPS," *Am. J. Otol.* **6**, 80-83 (1985).

[11] J. P. Wilson and J. R. Johnstone, "Basilar Membrane and Middle Ear Vibration in the Guinea Pig Measured by a Capacitive Probe," *J. Acoust. Soc. Am.* **57**, 705-723 (1975).

[12] P. Gilad, S. Shtrikman, P. Hillman, M. Rubenstein, and A. Eviator, "Application of the Mössbauer Method to Ear Vibrations," *J. Acoust. Soc. Am.* **41**, 1232-1236 (1967).

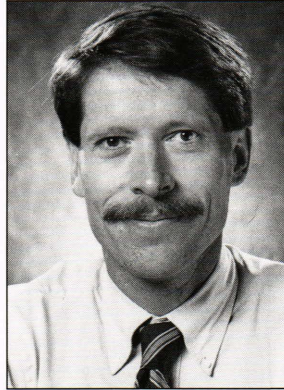[13] P. R. Dragsten, W. W. Webb, J. A. Paton, and R. R. Capranica, "Light-

Scattering Heterodyne Interferometer for Vibration Measurements in Auditory Organs," *J. Acoust. Soc. Am.* **60**, 665-671 (1976).

[14] J. Tonndorf and S. M. Khanna, "The Role of the Tympanic Membrane in Middle Ear Transmission," *Annals Oto.* **79**, 743-53 (1970).

[15] C. J. Brenkman, W. L. C. Rutten, and J. J. Grote, "Middle Ear Research using a SQUID Magnetometer II. Transfer Characteristics of Human Middle Ears," Lecture notes on Biomathematics, Peripheral Auditory Mechanisms, J. G. Allen, J. L. Hall, A. Hubbard, S. T. Neely, and A. Tubis, eds., Springer-Verlag, New York, pp. 56-59 (1986).

[16] K. Gyo, H. Aritomo, and R. L. Goode, "Measurement of Ossicular Vibration Ratio in Human Temporal Bones by Use of a Video Measuring System," *Acta Otolaryngol.* **103** 87-95 (1987).

[17] A. D. Drake and D. C. Leiner, "A Fiber Fizeau Interferometer for Measuring Minute Biological Displacements," *IEEE Trans. Biomed. Eng.* **7**, 507-511 (1984).

[18] W. H. Steel, *Interferometry*, 2nd ed., Cambridge Studies in Modern Optics, Cambridge University Press, Cambridge (1985).

[19] T. Kwaaitaal, B. J. Luymes, and G. A. van der Pijll, "Noise Limitations of Michelson Interferometers," *J. Phys, D.: Applied Phys.* **13**, 1005-1015 (1980).

[20] I. P. Kaminow, "Polarization in Optical Fibers," *IEEE J. Quantum Electron.* **QE-17**, 15-21 (1981).

[21] R. Ulrich, S. C. Rashleigh, and W. Eickhoff, "Bending-Induced Birefringence in Single-Mode Fibers," *Opt. Lett.* **5**, 273-275 (1980).

[22] H. C. Lefevre, "Single-Mode Fibre Fractional Wave Devices and Polarisation Controllers," *Electron. Lett.* **16**, 778-780 (1980).

[23] M. S. M. G. Vlaming and L. Feenstra, "Studies on the Mechanics of the Normal Human Ear," *Clin. Otolaryngol.* **11**, 353-363 (1986).

[24] P. Wade, M. A. Gresty, and L. J. Findley, "A Normative Study of Postural Tremor of the Hand," *Arch. Neurol.* **39**, 358-362 (1982).

THE AUTHOR

DONALD D. DUNCAN is Supervisor of the Measurements and Propagation Section of APL's Electro-Optical Systems Group. He received a Ph.D. in electrical engineering from Ohio State University in 1977. During 1977-83, he was employed by Pacific-Sierra Research Corp., where he performed modeling of optical propagation phenomena such as aerosol scatter, atmospheric turbulence, and high-energy laser effects (thermal blooming, aerosol burn-off). Since joining APL in 1983, Dr. Duncan has worked on various biomedical engineering projects, provided test program support and data analysis for a tracking/guidance synthetic aperture radar system, and worked on a variety of measurement, modeling, and diagnostic equipment projects in support of the hypersonic interceptor. He teaches courses in Fourier and statistical optics at The Johns Hopkins University.